AIP | The Journal of
Chemical Physics

Exploring surface photoreaction dynamics using pixel imaging mass spectrometry (PImMS)

Matthew D. Kershis, Daniel P. Wilson, Michael G. White, Jaya John John, Andrei Nomerotski et al.

Citation: J. Chem. Phys. **139**, 084202 (2013); doi: 10.1063/1.4818997
View online: http://dx.doi.org/10.1063/1.4818997
View Table of Contents: http://jcp.aip.org/resource/1/JCPSA6/v139/i8
Published by the AIP Publishing LLC.

THE JOURNAL OF CHEMICAL PHYSICS **139**, 084202 (2013)

Exploring surface photoreaction dynamics using pixel imaging mass spectrometry (PImMS)

Matthew D. Kershis,[1] Daniel P. Wilson,[1] Michael G. White,[1,2,a)] Jaya John John,[3]
Andrei Nomerotski,[3,4] Mark Brouard,[5] Jason W. L. Lee,[6] Claire Vallance,[6]
and Renato Turchetta[7]
[1]*Department of Chemistry, Stony Brook University, Stony Brook, New York 11794, USA*
[2]*Chemistry Department, Brookhaven National Laboratory, Upton, New York 11973, USA*
[3]*Department of Physics, University of Oxford, Oxford OX1 3RH, United Kingdom*
[4]*Physics Department, Brookhaven National Laboratory, Upton, New York 11973, USA*
[5]*The Department of Chemistry, University of Oxford, The Physical and Theoretical Chemistry Laboratory, South Parks Road, Oxford OX1 3QZ, United Kingdom*
[6]*The Department of Chemistry, University of Oxford, Chemistry Research Laboratory, 12 Mansfield Road, Oxford OX1 3TA, United Kingdom*
[7]*Rutherford Appleton Laboratory, Didcot OX11 0QX, United Kingdom*

(Received 27 June 2013; accepted 7 August 2013; published online 26 August 2013)

A new technique for studying surface photochemistry has been developed using an ion imaging time-of-flight mass spectrometer in conjunction with a fast camera capable of multimass imaging. This technique, called pixel imaging mass spectrometry (PImMS), has been applied to the study of butanone photooxidation on $TiO_2(110)$. In agreement with previous studies of this system, it was observed that the main photooxidation pathway for butanone involves ejection of an ethyl radical into vacuum which, as confirmed by our imaging experiment, undergoes fragmentation after ionization in the mass spectrometer. This proof-of-principle experiment illustrates the usefulness and applicability of PImMS technology to problems of interest within the surface science community. © *2013 AIP Publishing LLC*. [http://dx.doi.org/10.1063/1.4818997]

I. INTRODUCTION

Since the pioneering work performed by Chandler and Houston[1] and Eppink and Parker,[2] velocity map imaging experiments have been used extensively for elucidating gas phase reaction dynamics occurring at the molecular level.[3] Although the technique was initially used to study gas-phase reactions, several groups have used this approach to study reaction dynamics at surfaces.[4–14]

A common feature to all of these studies is the use of a time-of-flight mass spectrometer (TOF-MS) that is capable of spatially separating ions based upon differences in kinetic energy and trajectory. By using ion optics capable of velocity-vector focusing, ions with a common velocity and trajectory are focused to the same spot on the detector, typically a microchannel plate (MCP) coupled to a phosphor screen. Images of the phosphor screen captured during the experiment can then be analyzed to yield dynamical information about the reaction. While this feature is useful in gas phase experiments for discriminating amongst reaction products with different internal state distributions, surface scientists can use this technique to determine the angular distribution of molecules and/or molecular fragments desorbing from a surface. For reactions which produce multiple products, differences in ion time-of-flight can be exploited to allow for the imaging of different species. Traditionally, the imaging of multiple products is accomplished by applying a time-gate to the TOF-MS detector, whereby the detector is switched on during the expected arrival time window of the mass of interest and is switched off at all other times during the experiment. This procedure is then repeated for imaging other masses. While this is certainly an effective means of conducting a comprehensive imaging study of multiple reaction species, it can prove to be highly time consuming. This is particularly true for surface science experiments, since surface cleaning and preparation in between measurements leads to additional down time.

For the study of complex photoreactions which yield multiple products, it is highly advantageous to use techniques which allow for the imaging of multiple masses during a single experiment without mass gating. As a result of advances in image sensor technology, multiple mass image capture is now possible using sensor arrays capable of multi-hit, time-resolved detection at individual pixels on a time scale of tens of nanoseconds.[15–18] The combination of mass spectrometry using velocity vector focusing and time-resolved image capture, so-called pixel imaging mass spectrometry (PImMS), has recently been applied to the study of gas-phase fragmentation processes[19] as well as to spatial imaging mass spectrometry.[20] As demonstrated in this work, the PImMS technique is especially useful for analogous *surface* photochemistry experiments involving multiple mass photoproducts.

[a)] Author to whom correspondence should be addressed. Electronic mail: mgwhite@bnl.gov. Telephone: (631) 344-4345. Fax: (631) 344-5815.

In this experiment, we use the PImMS technique to study the ultraviolet (UV)-induced photooxidation of 2-butanone (methyl ethyl ketone) on a $TiO_2(110)$ single crystal surface. These experiments are motivated by the widespread use of titania as a photocatalyst for the degradation of organic pollutants from air and water environments.[21–23] Previous work has shown that under UHV conditions, multiple photoproducts are ejected into vacuum (methyl and ethyl radicals, molecular oxygen) upon irradiating adsorbed butanone-oxygen adlayers with ultraviolet light.[24,25] Particularly for the case of ethyl radical desorption, multiple, closely spaced mass peaks (m/z: 27–29) are observed in product mass spectra, which are assumed to be $C_2H_x^+$ hydrocarbon fragments ($x = 3, 4, 5$). Initial studies by Henderson[24] assigned these C_2H_x fragments to primary and secondary reaction products, whereas a recent pump-probe study by Wilson *et al.*,[25] suggests that all the mass fragments are associated with direct ethyl ejection without secondary collisions. In this work, we show how PImMS technology can be applied to surface photochemistry experiments and use it to gain additional insights into the dynamical origins of the C_2H_x photofragments from butanone photooxidation.

II. EXPERIMENTAL

A. Overview

A schematic diagram of the experimental setup is shown in Figure 1. The $TiO_2(110)$ surface dosed with adsorbates is irradiated by a UV pump laser beam (335 nm; 3.70 eV) at an incident angle of 45°. Neutral fragments coming from the surface travel a free flight distance of 29.4 mm before being ionized by the coherent vacuum ultraviolet (VUV) radiation (94.7 nm; 13.09 eV) which passes parallel to the surface plane in the center of the acceleration region of an imaging TOF-MS. The ions are accelerated by the lens elements and detected ~40 cm downstream by a dual MCP detector and phosphor screen. A sealed enclosure surrounds the phosphor outside of the chamber to minimize light contamination from the laboratory. Due to space restrictions, the PImMS camera was mounted outside of this enclosure. A piece of PVC (polyvinyl chloride) tubing was used to couple the camera to the enclosure and a mirror placed in front of the phosphor directed the images to the camera sensor. In addition to the PImMS camera, a photomultiplier tube (PMT) was placed inside the enclosure, enabling signal from the phosphor to be measured when performing conventional TOF-MS experiments.

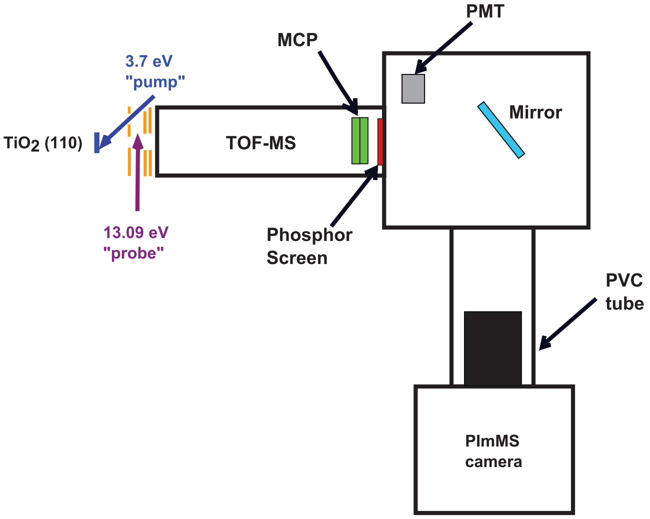

FIG. 1. Schematic diagram of the experimental setup. The prepared sample is placed in front of our TOF-MS and is irradiated by the pump laser that strikes the surface via openings in the extractor front and the repeller lenses. Neutral fragments ejected from the surface travel a distance of 29.4 mm into the ionization region of the mass spectrometer where they are ionized by the probe laser after a fixed time delay. The ionized parent (and fragment) ions are focused onto specific locations on the detector based upon their initial trajectory. Images of the phosphor are recorded by the PImMS camera that records both mass spectrometric data and images simultaneously.

B. General experimental methods

Experiments were carried out in a two-tier UHV chamber which has been described in detail elsewhere.[26] The UHV chamber had a base pressure of $< 3 \times 10^{-10}$ Torr and was connected to a smaller chamber[27] that was used for generation of VUV radiation. The two chambers were connected via a doubly differentially pumped capillary tube which allowed for passage of VUV light into the main chamber while maintaining a factor $\sim 10^8$ difference in pressure between the VUV-generation and UHV chambers. A custom-built TOF-MS is mounted in the lower level of the UHV chamber, which also contains a directional doser used to deposit organic molecules on the titania surface. The upper level of the main chamber houses a sputter gun, quadrupole mass spectrometer (QMS, Hiden Analytical) for temperature programmed desorption measurements (TPD), and a low energy electron diffraction (LEED, Princeton Research) apparatus for confirming long-range surface order.

The rutile $TiO_2(110)$ single crystal ($10 \times 10 \times 2$ mm) was obtained from CrysTec and was initially prepared by high energy, high temperature sputtering (2 keV, 800 K) and annealing (850 K) cycles. This treatment produced a crystal which had undergone a significant amount of bulk reduction as evidenced by its dark blue color.[28] Routine surface preparation consisted of low energy sputtering (0.5 keV, 10 min) and annealing (850 K, 30 min). The crystal was oriented so that the [001] direction was parallel to the probe beam direction and mounted to a liquid nitrogen-cooled manipulator in a manner as described previously.[25]

Prior to photochemistry experiments, the titania surface was exposed to 80 L of oxygen followed by ~1 ML of butanone. Research grade oxygen (Matheson Tri-Gas) was used without further purification, while butanone (Sigma-Aldrich) was purified by multiple pump-freeze-thaw cycles. Oxygen was admitted to the surface by backfilling the chamber and butanone gas was deposited on the surface using a directional doser. Prior to beginning a measurement, the surface was heated to a temperature of ~200 K to enhance the ethyl radical signal as observed in previous work.[25] Additionally, photochemistry experiments were conducted in a background atmosphere of oxygen (5×10^{-8} Torr) to further enhance signal levels. By comparing our TPD data to the results published by Henderson,[24] we estimate our butanone coverage at ∼200 K to be less than ∼1 ML. Due to the relatively high background pressure of oxygen used in these experiments, the MCP detector was gated so that the large O_2 signal did not damage the detector or saturate the camera sensor.

Pump-probe laser techniques were used to generate and ionize neutral gas-phase species. The pump laser (335 nm, 3.7 eV) was a Nd:YAG-pumped optical parametric oscillator (OPO) system (Spectra-Physics Lab 150, GWU/Lasertechnik versaScan with uvScan option). The diverging UV output beam was collimated by a cylindrical telescope, and apertures close to the chamber were used to further reduce the beam size. The pump beam struck the crystal at an angle of 45° resulting in an irradiated area of 0.5 cm^2. Prior to entering the chamber, the laser passed through a pair of Glan-Thompson polarizers (Lambrecht) which served to control photon flux and to establish p-polarized light relative to the crystal face. The photon flux was attenuated further by using calibrated neutral density filters. For this experiment, the photon fluence of the pump beam was $\sim 3.4 \times 10^{14}$ photons $\mathrm{cm}^{-2}\,\mathrm{s}^{-1}$ (calculated by multiplying the pulse flux by the 20 Hz laser repetition rate).

The probe laser was a Nd:YAG-pumped dye laser (Spectra-Physics GCR-230, LDL 20505 with Rhodamine 590 dye) whose visible output (568.42 nm) was frequency doubled to produce 284.21 nm light. The UV output from the probe laser was directed into the VUV chamber and tightly focused in front of a pulsed valve which directed a jet of N_2 gas into the chamber. VUV radiation was produced by third-harmonic generation (THG) in N_2 gas.[29] The resulting 94.74 nm (13.09 eV) light was captured by a capillary light guide and directed into the main chamber and into the ionization region of the TOF-MS.

C. Velocity vector focusing TOF-MS for surface photochemistry

In these experiments, we used a TOF-MS that is capable of velocity vector focusing, i.e., ions created in the ionization region of the mass spectrometer are directed toward specific points on the MCP detector based upon their initial velocity vector. A key advantage of velocity focusing for surface studies is that the entire sample surface can be irradiated with an unfocused laser beam (pump) without degrading the quality of the downstream ion image. This allows us to keep the laser fluence on the surface to a minimum to avoid surface damage and limit multiphoton effects, while at the same time sampling the maximum number of absorbates for good signal levels. Second, we can use an unfocused VUV laser beam for "universal" neutral product detection, which is particularly advantageous for detecting polyatomic species, e.g., small hydrocarbon radicals, whose excited states are not known and thereby not readily amenable to resonant multiphoton ionization (REMPI) techniques.[25] Ionization by an unfocused VUV beam provides a large acceptance angle for intercepting neutral products along the VUV beam direction, but results in a line source of ions that would yield a spatially "smeared" angular distribution without vector focusing. Unlike gas-phase experiments, the pump and probe laser beams are not spatially overlapped, since both beams are likely to interact strongly with the substrate and/or adsorbates at the surface. In our design, the spatial separation of the UV pump and VUV probe beams (25–30 mm) is a compromise between optimizing the detection solid angle (short distance) and optimizing the velocity resolution of the pump-probe delay measurements (long distance). Hence, the main information we obtain from our surface velocity focusing experiments is the angular distribution of neutral products within a narrow velocity range as determined by the pump-probe laser delay and angular acceptance of the detector.

To be more specific, the pump-probe delay determines the longitudinal velocity component along the surface normal and parallel to the TOF analyzer axis. Hence, the use of short pump-probe delays results in the ionization of neutrals with higher velocities (larger kinetic energies) within a narrow range determined by the velocity resolution of the neutral detection step and the angular acceptance of the TOF analyzer. The velocity resolution of the detection step (∼ 14%) is determined primarily by the uncertainty in the neutral flight path, i.e., $\frac{\Delta\ell}{\ell}$, where $\Delta\ell$ is the length of the ionization region given by the VUV beam diameter (4 mm), and ℓ is the distance from the crystal surface to the ionization region (29.4 mm). The second part of the velocity spread comes from the fact that neutrals entering the TOF analyzer at non-zero angles have transverse velocity components perpendicular to the TOF axis (v_z). Since the pump-probe delay only selects the longitudinal component, this leads to the detection of neutrals with a range of velocities that are simply related to the acceptance angle of the TOF analyzer. With an acceptance angle of ± 30°, the spread in neutral velocities in the horizontal direction is ±13% of v_z. In terms of imaging, ions with larger transverse velocity components will be focused further from the center of the detector. Hence, ion images taken for "fast" neutrals corresponding to short pump-probe time delays will appear larger than images taken for "slow" neutrals at longer delays (assuming identical angular distributions). This instrumental dependence of image size on angular spread can be readily accounted for through the calculation of "detector functions" (see below) that allow the angular distributions of desorbing neutrals to be extracted from the images.

SIMION 3D was used to design the ion imaging electrodes that serve as the acceleration and focusing fields for ions born in the interaction region following VUV ionization. The main constraint of the design was the use of a line ionization source with a width of ∼2 cm, which provides a large acceptance solid angle (± 30°) for reasonably sized focusing elements. A 3D rendering of the accelerating and focusing elements is shown in Figure 2. The large 2 cm ion source in the horizontal direction required the use of thick lens elements with large apertures (V_2 and V_3; 40 mm ID, 16 mm thick) to tailor the electric fields for velocity focusing at the extreme edges. To compensate for the cut-out in the repeller electrode (V_1), which allows the UV beam to strike the crystal, a "horseshoe" electrode (V_4) was added to the back of the repeller plate. The UV light reflected off the crystal was intercepted by a small mirror attached to the back of the repeller plate (not shown) and directed away from the ion detector. The end of the glass capillary light guide was also enclosed

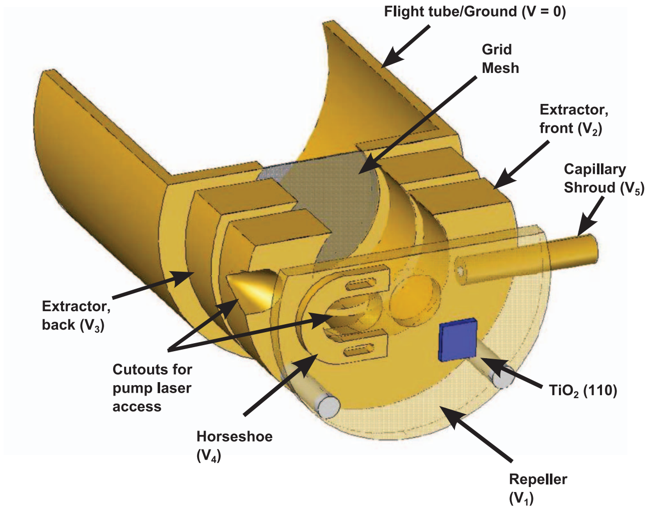

FIG. 2. Three-dimensional rendering of our imaging TOF-MS showing the imaging lenses as well as part of the flight tube. The TOF-MS has been sliced in the horizontal plane to better illustrate the geometry of the instrument.

in a metallic tube so that any distortion of the field caused by its insertion near the edge of the ionization region could be roughly compensated by applying a suitable potential (V_5). After being accelerated to 100 eV, ions exiting the final focusing lens (V_3) pass through a grounded grid and enter a field free region before striking the MCP detector. The overall flight distance from the ionization region to the end of the field free region is 40 cm. All the lens elements were made of oxygen-free high conductivity (OFHC) copper and electroplated with gold.

The detection geometry employed here imposes the limitation that only a subset of neutral trajectories is detected in each surface photodesorption experiment. Specifically, the use of a line ionization source downstream of the surface means that the neutral acceptance angle along the VUV beam axis, referred to as the "horizontal" direction, is larger than the acceptance angle perpendicular to the VUV beam axis, referred to as the "vertical" direction. As shown in more detail in Figure S1 in the supplementary material,[33] neutrals intersecting a 2 cm length of VUV beam results in a horizontal acceptance angle of about $\pm30°$, whereas the smaller VUV beam diameter of $\sim$4 mm restricts the vertical acceptance angle to $\pm12°$. These angles are defined relative to the surface normal. As noted earlier, the lens stack was optimized primarily to ensure ion vector focusing along the VUV beam axis (horizontal direction), since the larger range of acceptance angles provides more information on the spatial distribution of the desorbing neutrals.

In order to extract spatial information on the desorbing neutrals, it is necessary to relate the final position of the ion at the detector to the initial trajectory of the neutral photoproduct entering the TOF-MS. Because of the difference in horizontal and vertical acceptance angles, even a cylindrically symmetric angular distribution about the surface normal (detector axis) will generally appear elliptical, with the long axis along the horizontal (VUV beam) direction. Hence, the first step in extracting angular information involves the determination of the vertical and horizontal collection efficiencies (i.e., detector functions) as a function of ion trajectory angle and velocity. Details of the method used to determine the horizontal and vertical collection efficiency curves are given in Figure S3 in the supplementary material[33] along with calculated examples. These collection efficiency functions relate desorption angle to detector position (in mm), which in turn can be related to camera pixel.

D. PImMS camera

The PImMS camera has already been described in previous publications, and so only a brief discussion will be presented here.[15–20] The heart of the PImMS camera system is a 72 × 72 pixel array based on CMOS technology which is designed to capture the visible light image emitted from the phosphor screen. The PImMS sensor is set apart from conventional imaging cameras through its ability to record spatial and temporal information simultaneously for each detected particle. At the time of these experiments, the best available timing resolution was 25 ns, although 12.5 ns resolution is now achievable. Using a time resolution of 25 ns, data can be acquired for 102.4 μs per TOF cycle, determined by the 12-bit capacity of the pixel clock.[19]

III. RESULTS

Previous work[24] has shown that the main photooxidation pathway of 2-butanone on $TiO_2(110)$ proceeds via ejection of an ethyl radical (C_2H_5; mass 29) into vacuum. However, time-of-flight mass spectra showed the presence of masses at 26–28 amu in addition to ethyl radicals. The kinetic energy distributions obtained for masses 27, 28, and 29 were found to be bimodal ($\langle E_t(\text{fast})\rangle = 0.098$ eV, $\langle E_t(\text{slow})\rangle = 0.024$ eV) and it was observed that the three distributions were identical.[25] This result is indicative of masses 27–29 having the same neutral parentage, i.e., mass 27 and 28 result from the dissociative ionization of ethyl radical (mass 29) induced by VUV ionization at 13.09 eV.[30] Consequently, mass 27 and mass 28 ions correspond to $C_2H_3{}^+$ and $C_2H_4{}^+$ fragments. The time-of-flight spectra of all the gas-phase products resulting from 2-butanone photooxidation on $TiO_2(110)$ are presented in Figure 3 and are consistent with previously published results.[25] The spectrum in Figure 3(a) was recorded at a pump-probe laser delay of 59 μs (representative of "slow" ethyl radicals) and shows the presence of methyl radical, background water, and ethyl radical and its fragments. The spectrum in Figure 3(b) was taken at a 24.6 μs pump-probe laser delay (representative of "fast" ethyl radicals) and shows a similar product distribution. A small amount of photodesorbing oxygen (mass 32) is also seen. The latter arrives slightly before the background oxygen (as a result of its additional kinetic energy) and thus falls just outside of the gating pulse applied to the MCP detector. The $O_2{}^+$ signal is actually much larger than seen in Figure 3, but the MCP gate was chosen to eliminate a majority of this signal to prevent saturation of the MCP. The mass spectrum in Figure 3(b) shows a small peak for mass 26, whereas this feature is absent at longer pump-probe laser delays (Figure 3(a)). As a result of

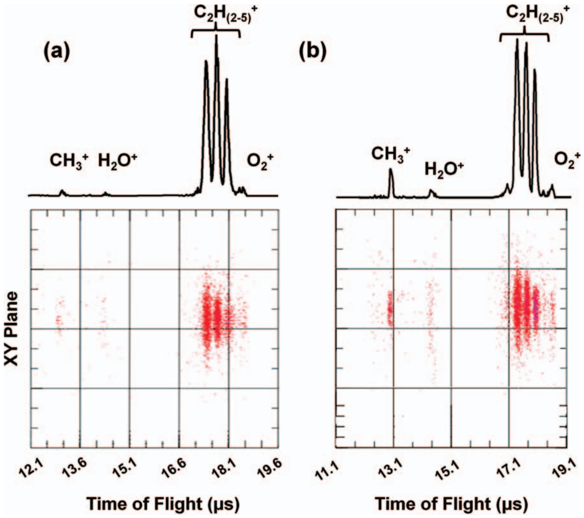

FIG. 3. Time-of-flight mass spectra taken for both (a) slow and (b) fast channels. Below each mass spectrum is the data in its 3D form where the horizontal axis represents time and the vertical axis represents the detector plane with units of pixels. The 3D images have been rotated slightly about the time axis to better illustrate the ion clouds. Thus, the vertical axes do not correspond to single detector axis (i.e., x or y) but rather some arbitrary combination of the two.

such small signal, it is not possible to provide any further insights into the origin of the mass 26 species, although the observed dependence of the signal on pump-probe laser delay suggests that it is not due to fragmentation of the ethyl radical photoproduct.[25] Signal due to methyl radical is significantly larger at the shorter laser delay consistent with the higher average kinetic energy for the methyl radical ($\langle E_t(\text{total})\rangle = 0.195$ eV) compared to ethyl radical ($\langle E_t(\text{total})\rangle = 0.051$ eV) produced by 2-butanone photooxidation.[31]

In addition to showing the product TOF-MS in Figs. 3(a) and 3(b), we have also included "4D" representations (which are functions of time, x pixel, y pixel, and signal intensity) of the data as recorded by the camera. The horizontal axis represents time whereas the vertical axis represents one of the camera's pixel directions (i.e., either x or y). The other pixel direction would be normal to the plane of the page and is thus not visible. In this representation, the spatial distribution of reaction products as a function of flight time can be easily visualized. For the $C_2H_{(2-5)}{}^+$ species, there is an obvious increase in spatial size going from high to low mass. As will be discussed below, this is due to fragmentation of the ethyl cation. Primary surface products (such as methyl and ethyl radicals) appear as tightly collimated distributions about the detector axis whereas background species (such as water) do not appear to be collimated at all.

Two-dimensional cuts through the PImMS data sets, yielding velocity-map images for ethyl radical and its fragments, are shown in Figure 4. The images in Figure 4(a) were taken at a pump-probe laser delay of 59 μs, while those in Figure 4(b) were taken at a laser delay of 24.6 μs. These laser delays correspond to ionization of the "slow" and "fast" fragments, respectively. As noted earlier, ion images taken at different laser delays will generally have different sizes due to differences in the transverse velocity components of neutrals entering the ionization region with non-zero angles. This is clearly seen for mass 29, for which the image for the "slow"

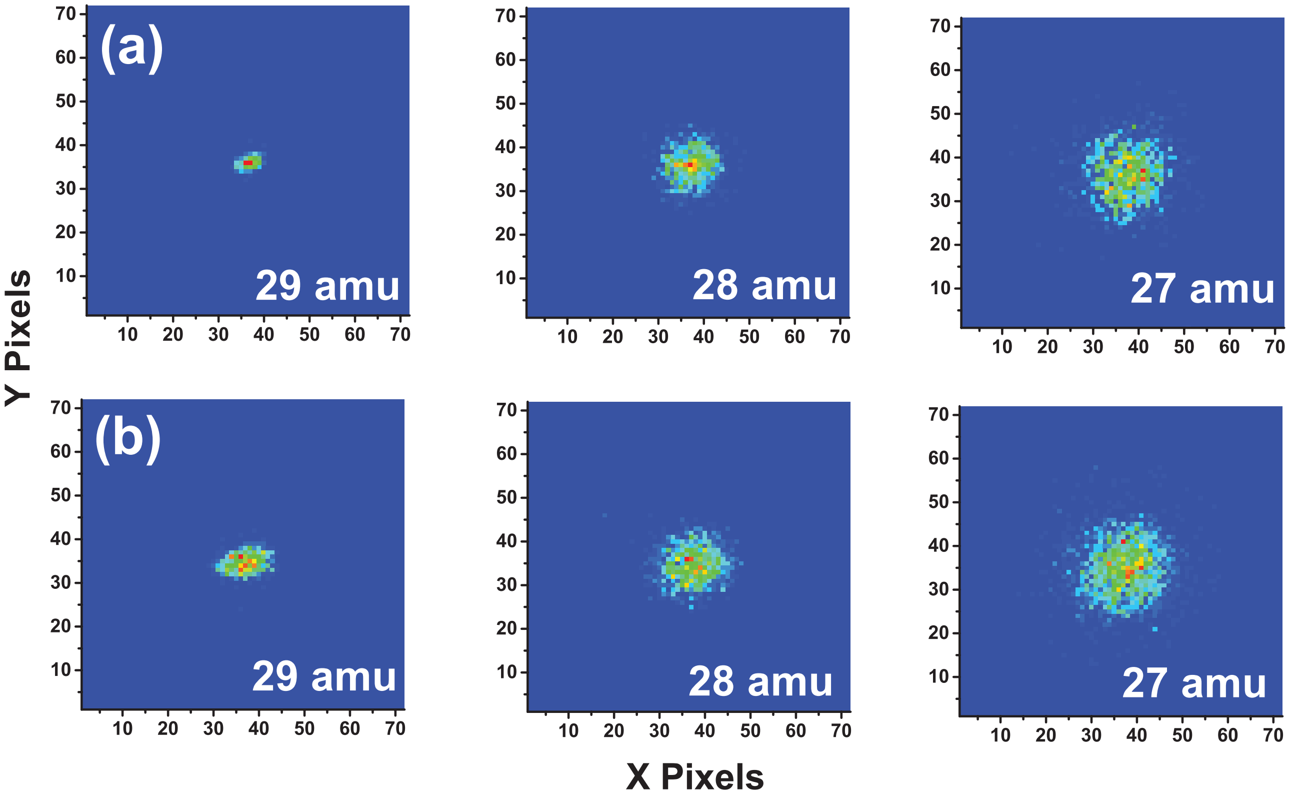

FIG. 4. Two-dimensional images of masses originating from ethyl radical and its fragments. Figure 4(a) shows images of (from left to right) ethyl radical (mass 29), mass 28, and mass 27 taken at a 59 μs laser delay. Figure 4(b) shows images of the same three masses but at a 24.6 μs laser delay.

ethyl fragments (Fig. 4(a)) is smaller than that for the "fast" ethyl fragments (Fig. 4(b)). Note that a similar increase in spatial extent is not observed for masses 27 and 28. More important is the increase in image size for the mass 27 and 28 fragments compared to the ethyl radical parent (mass 29) at either pump-probe delay. As noted above, previous pump-probe experiments have shown that all the three ion products (masses 27–29) exhibit the same velocity and translational energy distributions.[25] The velocity distributions of the various fragments are reflected in the radial distributions of the corresponding images. Hence, if masses 27, 28, and 29 were desorbed directly from the surface, one would expect that the images for all three masses should exhibit similar spatial distributions except for a scaling arising from the difference in mass. The increase in image size for masses 27 and 28 compared to mass 29 must then be due to differences in angular distributions and/or an increase in transverse energy spread. A change in angular distribution would suggest differences in neutral fragmentation dynamics for masses 27–29, whereas an increase in transverse momentum could result from dissociative ionization following VUV photoionization of the parent ethyl radical. As will be discussed in Sec. IV, it is possible to distinguish between signal resulting from direct photodesorption from the surface and signal resulting from fragmentation within the mass spectrometer.

IV. DISCUSSION

The detector functions not only allow us to extract angular distribution data from the 2D images, but are also useful for differentiating between contributions originating from the desorption of surface species and those arising from fragmentation that occurs after ionization. In Figure 5, horizontal cuts through the 2D images shown in Figure 4 are plotted along with the detector functions calculated for the relevant pump-probe laser delay and fragment mass. The experimental data shown in Figures 5(a) and 5(b) were taken at a pump-probe laser delay of 59 μs and 24.6 μs, respectively. As is seen in Figure 5, for a given choice of laser delay/ion velocity, the detector functions for masses 27–29 are practically identical. This is due to the fact that the difference in kinetic energy for these ions is small (∼3%–5%). While the images for mass 29 in Figures 4(a) and 4(b) are of different sizes depending on the ion's kinetic energy, this difference is not obvious when looking at the detector functions. This is because the detection probability, when presented as a function of desorption angle, must be the same regardless of the ion's initial kinetic energy. If this were not the case, it would be impossible to compare angular distributions for ions generated at different laser delays.

The data presented in Figure 5, which shows horizontal cross sections of the images in Figure 4, are helpful in understanding which species are due to photodesorption from the surface and which species are due to the fragmentation of primary photoproducts. The signal distribution obtained for mass 29 (ethyl radical) is seen to be significantly narrower than the calculated detector function for both laser delays. This shows that the horizontal acceptance of the imaging detector is not limiting the spatial extent of the observed images and also indicates that the angular distribution of the ethyl radicals leaving the surface is extremely narrow and peaked along the surface normal. This is not unexpected for a "prompt" photofragmentation process on the surface, in which the fragment, ethyl radical in this case, is ejected from the surface without secondary collisions.[32]

To gain some insight into the angular distribution of photodesorbing ethyl radicals, the images of mass 29 were analyzed to yield angular distributions for ethyl radicals desorbing in the horizontal direction (i.e., parallel to the [001] direction of the surface). Data from the 3 central rows of the

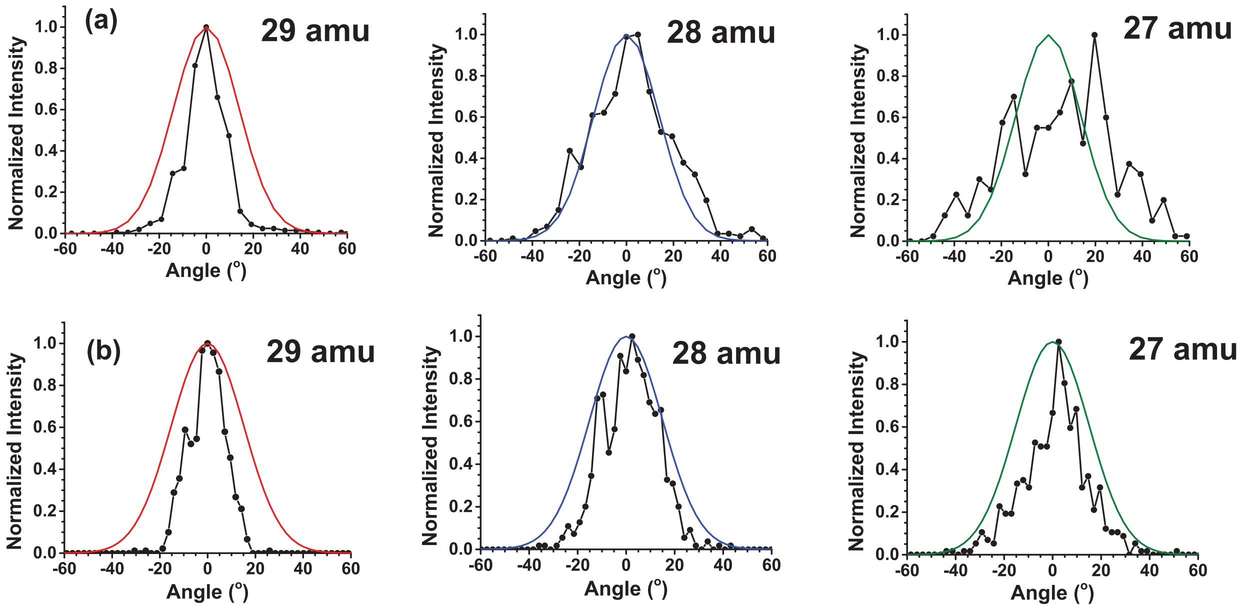

FIG. 5. Horizontal cross sections taken for images of masses 29–27 (left to right) at (a) 59 μs laser delay and (b) 24.6 μs laser delay. For data taken at the longer delay, the degree of fragmentation for ethyl radical is quite severe and there is signal which falls outside of the limits imposed by our detector function. Fragmentation does not appear to be as severe for data taken at the shorter delay, although there is a clear broadening of the distribution for masses 28 and 27.

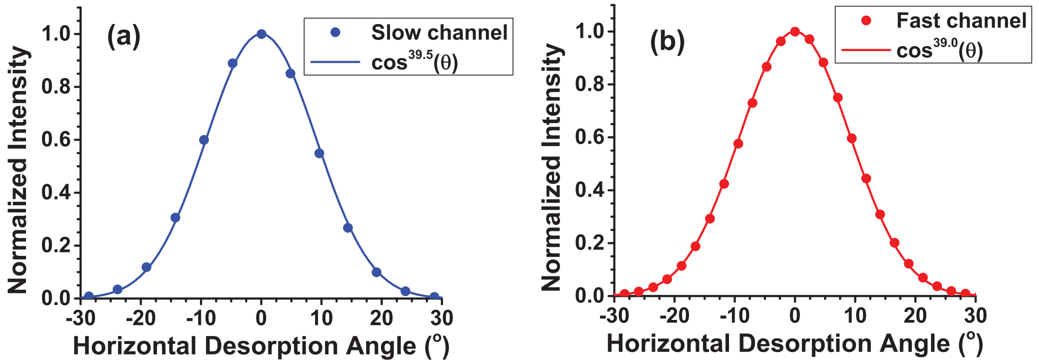

FIG. 6. Angular distributions of ethyl radical desorption for the (a) slow and (b) fast channels along with cos$^n(\theta)$ fits to the data. For the slow channel $n = 39.5$ and for the fast channel $n = 39.0$. The angular distribution of ethyl radicals is essentially the same for both kinetic energies studied in this work.

2D images for mass 29 were averaged together and plotted as a function of angle as shown in Figure 5. These raw data from $-30°$ to $+30°$ were fit to a Gaussian function of the form

$$S(\theta) = \mathrm{Aexp}\left[-\frac{1}{2}\left(\frac{\theta-\theta_o}{b}\right)^2\right],$$

where S represents signal intensity, A represents amplitude, θ_o represents the center angle of the distribution, and b represents the distribution width parameter. This fitted function was normalized and divided by the normalized detector function to yield the correct angular distribution for the "slow" channel (59 μs) shown in Figure 6(a) and for the "fast" channel (24.6 μs) shown in Figure 6(b). There are more data points for the fast channel because, as previously described, the faster ions are not focused as tightly and thus occupy more space on the detector. This results in the angular distribution data being spread over a larger number of pixels and thus gives more data points for a given angular spread. As is common for the analysis of photodesorption angular distributions,[32] the data were fit to functions of the form cos$^n(\theta)$. It was found that $n = 39.5$ for the slow channel whereas $n = 39.0$ for the fast channel. The fact that these exponent values are nearly identical shows that the angular distributions for ethyl photofragments ejected from the surface do not depend on kinetic energy.

The ion images in Figure 4 also shed light on the origin of masses 27 and 28. As noted above, the larger spatial images of the mass 27 and 28 fragments relative to mass 29 could be due to differences in angular distributions or transverse velocity components induced by fragmentation in the ionization region. Previous work by Henderson[24] using electron impact ionization detection had assigned masses 27–29 to ionic fragments resulting primarily from ethane (C_2H_6) and ethylene (C_2H_4) which are formed via secondary reaction products of ethyl radicals on the hydroxylated titania surface. More recently, Wilson *et al.*,[25] using "soft" VUV ionization were able to show that neither ethane or ethylene are formed under UHV photooxidation conditions, and that dissociative ionization of the ethyl photoproduct was likely to be the source of fragments at masses 27 and 28. Additional support for the dissociative ionization mechanism is provided by the comparison of the experimental horizontal cuts for masses 27 and 28 and the calculated detector functions shown in Figure 5. In the case of dissociative ionization, we expect the daughter fragments to gain transverse momentum relative to the motion of the neutral parent, depending on the dynamics of the ionic fragmentation process induced by VUV photoionization. The spatial and energy distribution of the daughter fragments will depend on the lifetime and excess energy of the excited cation intermediate (ethyl radical ion), and fragments moving transverse to the ethyl radical direction would be expected. Hence, daughter ions resulting from dissociative ionization of ethyl radical should exhibit broader angular distribution than the parent ion. At both pump-probe laser delays, the horizontal angular distributions broaden with decreasing mass. This observation is consistent with a sequential dissociative ionization mechanism in which the formation of mass 27 has experienced two fragmentation events and consequently more transverse "kicks" than mass 28, or by a single-step dissociation in which a fragment of higher mass (H_2 for mass 27 as opposed to H for mass 28) is ejected. The most convincing evidence of dissociative ionization comes from the mass 27 image at the longer pump-probe delay (59 μs). In this image, the experimental horizontal angular distribution extends to angles as large as ± 60°, which are beyond the limits of the detector function. Since it is physically impossible for a neutral fragment originating from the surface to reach the detector at angles larger than 30°, mass 27 must result from fragmentation within the mass spectrometer, i.e., from dissociative ionization. In the case of mass 28, dissociative ionization leads to broader angular distributions than the ethyl parent ion, but still within the acceptance limits of the detector. Nonetheless, the combination of angular broadening and our earlier final state energy distributions provides strong evidence that mass 28 is also a daughter fragment of the primary ethyl radical photoproduct.

V. CONCLUSIONS

The results presented in this paper are in close agreement with those of previous pump-probe studies of 2-butanone photooxidation on $TiO_2(110)$, which used measurements of final state energy distributions to conclude that the three product ions with masses 27–29 originate from a common neutral photoproduct, i.e., ethyl radical, via dissociative ionization.[24,25] While the use of final-state information can provide fairly conclusive evidence of parent ion fragmentation, the ion imaging approach demonstrated in this work provides an effective alternative and has the added benefit of providing the necessary data in a fraction of the time. In particular, the use of the PImMS technique allows us to explore the spatial distribution of multiple ions simultaneously, and thereby increases the amount of data that can be obtained in a single experiment. This is especially important for surface photochemistry experiments in which the photoactive sample on the surface is fixed and consumed during the measurement. For example, final state measurements of individual masses in a pump-probe experiment require multiple runs, each of which requires a new sample dose onto the crystal, and in some cases also requires crystal cleaning in between runs. By comparison, the sample in a gas-phase photochemistry experiment is essentially continuous, so data acquisition and signal averaging are much less constrained. The ability of the PImMS camera to provide temporal and spatial information for all photoproducts simultaneously allows certain quantitative comparisons to be made for data obtained within a single run. This is typically not possible when taking data on different days because of variations in experimental conditions. The multi-mass imaging capabilities of the PImMS camera provide a significant enhancement in the ability to study the dynamics of complex surface photoreactions such as 2-butanone photooxidation on TiO_2(110).

ACKNOWLEDGMENTS

The authors gratefully acknowledge Dr. Raj Rao and Dr. Joel Carney for their work with regard to the construction of the imaging TOF-MS and the development of the SIMION simulations. This work was carried out in the Chemistry Department at Brookhaven National Laboratory under Contract No. DE-AC02-98CH10086 with the (U.S.) Department of Energy (DOE) (Division of Chemical Sciences). The support of the Engineering and Physical Sciences Research Council (U.K.) EPSRC(GB) via Programme Grant No. EP/G00224X/1 (M.B. and C.V.), the European Union (EU) through grant FP7ITN "ICONIC" (Project Grant No. 238671 to M.B. and C.V.), STFC through a PNPAS award to A.N., M.B., C.V., and R.T., STFC through a mini-IPS grant ST/J002895/1 to A.N. and R.T., ERC through Starting Independent Researcher grant "ImageMS" (C.V.), and a "proof of concept" grant from ISIS Innovation Ltd. (M.B., C.V., and A.N.) are gratefully acknowledged.

[1] D. W. Chandler and P. L. Houston, J. Chem. Phys. **87**(2), 1445–1447 (1987).

[2] A. Eppink and D. H. Parker, Rev. Sci. Instrum. **68**(9), 3477–3484 (1997).

[3] M. N. R. Ashfold, N. H. Nahler, A. J. Orr-Ewing, O. P. J. Vieuxmaire, R. L. Toomes, T. N. Kitsopoulos, I. A. Garcia, D. A. Chestakov, S. M. Wu, and D. H. Parker, Phys. Chem. Chem. Phys. **8**(1), 26–53 (2006).

[4] Y. Y. Ji, S. P. K. Koehler, D. J. Auerbach, and A. M. Wodtke, J. Vac. Sci. Technol. A **28**(4), 807–813 (2010).

[5] M. Menges, B. Baumeister, K. Alshamery, H. J. Freund, C. Fischer, and P. Andresen, Surf. Sci. **316**(1–2), 103–111 (1994).

[6] M. Wilde, K. Fukutani, Y. Murata, M. Kampling, K. Al-Shamery, and H. J. Freund, Surf. Sci. **427–428**, 27–33 (1999).

[7] A. R. Burns, E. B. Stechel, and D. R. Jennison, Surf. Sci. **280**(3), 359–368 (1993).

[8] A. R. Burns, Surf. Sci. **280**(3), 349–358 (1993).

[9] D. Corr and D. C. Jacobs, Rev. Sci. Instrum. **63**(3), 1969–1972 (1992).

[10] P. H. Kobrin, G. A. Schick, J. P. Baxter, and N. Winograd, Rev. Sci. Instrum. **57**(7), 1354–1362 (1986).

[11] S. P. K. Koehler, Y. Y. Ji, D. J. Auerbach, and A. M. Wodtke, Phys. Chem. Chem. Phys. **11**(35), 7540–7544 (2009).

[12] M. Reid and S. P. K. Koehler, Rev. Sci. Instrum. **84**(4), 044101 (2013).

[13] J. R. Roscioli, D. J. Bell, D. J. Nelson, and D. J. Nesbitt, Phys. Chem. Chem. Phys. **14**(12), 4070–4080 (2012).

[14] J. R. Roscioli and D. J. Nesbitt, Faraday Discuss. **150**, 471–479 (2011).

[15] A. Nomerotski, M. Brouard, E. Campbell, A. Clark, J. Crooks, J. Fopma, J. J. John, A. J. Johnsen, C. Slater, R. Turchetta, C. Vallance, E. Wilman, and W. H. Yuen, J. Instrum. **5**, C07007 (2010).

[16] J. J. John, M. Brouard, A. Clark, J. Crooks, E. Halford, L. Hill, J. W. L. Lee, A. Nomerotski, R. Pisarczyk, I. Sedgwick, C. S. Slater, R. Turchetta, C. Vallance, E. Wilman, B. Winter, and W. H. Yuen, J. Instrum. **7**, C08001 (2012).

[17] M. Brouard, E. K. Campbell, A. J. Johnsen, C. Vallance, W. H. Yuen, and A. Nomerotski, Rev. Sci. Instrum. **79**(12), 123115–123118 (2008).

[18] I. Sedgwick, A. Clark, J. Crooks, R. Turchetta, L. Hill, J. J. John, A. Nomerotski, R. Pisarczyk, M. Brouard, S. H. Gardiner, E. Halford, J. Lee, M. L. Lipciuc, C. Slater, C. Vallance, E. S. Wilman, B. Winter, and W. H. Yuen, "PImMS: A self-triggered, 25ns resolution monolithic CMOS sensor for Time-of-Flight and Imaging Mass Spectrometry," New Circuits and Systems Conference (NEWCAS), 2012 IEEE 10th International, 497–500 (2012).

[19] A. T. Clark, J. P. Crooks, I. Sedgwick, R. Turchetta, J. W. L. Lee, J. J. John, E. S. Wilman, L. Hill, E. Halford, C. S. Slater, B. Winter, W. H. Yuen, S. H. Gardiner, M. L. Lipciuc, M. Brouard, A. Nomerotski, and C. Vallance, J. Phys. Chem. A **116**(45), 10897–10903 (2012).

[20] M. Brouard, E. Halford, A. Lauer, C. S. Slater, B. Winter, W. H. Yuen, J. J. John, L. Hill, A. Nomerotski, A. Clark, J. Crooks, I. Sedgwick, R. Turchetta, J. W. L. Lee, C. Vallance, and E. Wilman, Rev. Sci. Instrum. **83**(11), 114101 (2012).

[21] M. A. Fox and M. T. Dulay, Chem. Rev. **93**, 341–357 (1993).

[22] M. R. Hoffmann, S. T. Martin, W. Choi, and D. W. Bahnemann, Chem. Rev. **95**(1), 69–96 (1995).

[23] A. Fujishima, X. Zhang, and D. A. Tryk, Surf. Sci. Rep. **63**(12), 515–582 (2008).

[24] M. A. Henderson, Surf. Sci. **602**(20), 3188–3193 (2008).

[25] D. P. Wilson, D. P. Sporleder, and M. G. White, J. Phys. Chem. C **117**(18), 9290–9300 (2013).

[26] L. Fleck, B. Niu, R. J. Beuhler, and M. G. White, in Laser Techniques for Surface Science II, edited by J. M. Hicks, W. Ho, and H.-L. Dai, Proc. SPIE **2547**, 298–309 (1995).

[27] R. G. Tonkyn and M. G. White, Rev. Sci. Instrum. **60**(7), 1245–1251 (1989).

[28] M. Li, W. Hebenstreit, U. Diebold, A. M. Tyryshkin, M. K. Bowman, G. G. Dunham, and M. A. Henderson, J. Phys. Chem. B **104**(20), 4944–4950 (2000).

[29] R. H. Page, R. J. Larkin, A. H. Kung, Y. R. Shen, and Y. T. Lee, Rev. Sci. Instrum. **58**(9), 1616–1620 (1987).

[30] B. L. FitzPatrick, M. Maienschein-Cline, L. J. Butler, S. H. Lee, and J. J. Lin, J. Phys. Chem. A **111**(49), 12417–12422 (2007).

[31] D. P. Wilson, D. Sporleder, and M. G. White, Phys. Chem. Chem. Phys. **14**(39), 13630–13637 (2012).

[32] V. P. Holbert, S. J. Garrett, P. C. Stair, and E. Weitz, Surf. Sci. **346**(1–3), 189–205 (1996).

[33] See supplementary material at http://dx.doi.org/10.1063/1.4818997 for additional details regarding the imaging TOF-MS and the image analysis.